

## RADIO INTERFEROMETRIC OBSERVATION OF AN ASTEROID OCCULTATION

JORMA HARJU,<sup>1,2</sup> KIMMO LEHTINEN,<sup>3</sup> JONATHAN ROMNEY,<sup>4</sup> LEONID PETROV,<sup>5</sup> MIKAEL GRANVIK,<sup>6,7</sup>  
 KARRI MUINONEN,<sup>1,3</sup> UWE BACH,<sup>8</sup> AND MARKKU POUTANEN<sup>3</sup>

<sup>1</sup>*Department of Physics, P.O. BOX 64, 00014 University of Helsinki, Finland*

<sup>2</sup>*Max-Planck-Institut für extraterrestrische Physik, Gießenbachstraße 1, 85748 Garching, Germany*

<sup>3</sup>*Finnish Geospatial Research Institute FGI, Geodeetinrinne 2, FI-02430 Masala, Finland*

<sup>4</sup>*Long Baseline Observatory, 1003 Lopezville Road, Socorro, NM, 87801, U.S.A*

<sup>5</sup>*Astrogeo Center, Falls Church, U.S.A.*

<sup>6</sup>*Department of Computer Science, Electrical and Space Engineering, Luleå University of Technology, Box 848, S-981 28 Kiruna, Sweden*

<sup>7</sup>*Department of Physics, P.O. Box 64, 00014 University of Helsinki, Finland*

<sup>8</sup>*Max-Planck-Institut für Radioastronomie, Auf dem Hügel 69, 53121 Bonn, Germany*

## ABSTRACT

The occultation of the radio galaxy 0141+268 by the asteroid (372) Palma on May 15, 2017 was observed using six antennas of the Very Long Baseline Array (VLBA). The shadow of Palma crossed Brewster, Washington. Owing to the wavelength used, and the size and the distance of the asteroid, a diffraction pattern in the Fraunhofer regime was observed. The measurement retrieves both the *amplitude* and the *phase* of the diffracted electromagnetic wave. This is the first astronomical measurement of the phase shift caused by diffraction. The maximum phase shift is sensitive to the effective diameter of the asteroid. The bright spot at the shadow's center, the so called Arago-Poisson spot, is clearly detected in the amplitude time-series, and its strength is a good indicator of the closest angular distance between the center of the asteroid and the radio source. We also find that an amplitude versus phase diagram is useful for constraining the shape of the asteroid silhouette at the time of the occultation. Our modelling results suggest that the silhouette is slightly elongated and has a concave edge. A sample of random shapes constructed using a Markov chain Monte Carlo algorithm suggests that the silhouette of Palma deviates 10–20% from a perfect circle. The obtained effective diameter for Palma,  $192.1 \pm 4.8$  km, is in excellent agreement with recent estimates from thermal modeling of mid-infrared photometry. Finally, our computations show that because of the high positional accuracy, a single radio interferometric occultation measurement can reduce the long-term ephemeris uncertainty by an order of magnitude.

*Keywords:* techniques: interferometric — minor planets, asteroids: general — minor planets, asteroids: individual (372 Palma)

## 1. INTRODUCTION

Observations of lunar occultations provided the first accurate positions for compact extragalactic radio sources, and contributed to the discovery of quasars (Hazard et al. 1963; Schmidt 1963; Oke 1963). Lunar occultations have also been used to derive high-resolution images of radio sources from the Fresnel diffraction fringes observed with single-dish telescopes (e.g., Hazard et al. 1967; Maloney & Gottesman 1979; Schloerb & Scoville 1980; Cernicharo et al. 1994). Restoring techniques developed by Scheuer (1962) and von Hoerner (1964) were utilized in these works. More recently, the brightness distributions of compact radio sources have mainly been studied using interferometric arrays including Very Long Baseline Interferometry (VLBI). Nevertheless, radio occultations by solar system bodies remain useful for determining the properties of the *foreground* objects, including planetary atmospheres and coronal mass ejections from the Sun (Withers & Vogt 2017; Kooi et al. 2017).

One application of radio occultations is the possibility of determining the size of an asteroid by a single, short measurement. Together with the mass, obtainable from orbital deflections during close encounters, the size is needed for estimating the density, which in turn contains information of the composition and internal structure of an asteroid (Carry 2012). The radio occultation method was demonstrated by Lehtinen et al. (2016) who used the 100-m Effelsberg telescope to observe the occultation of a radio galaxy by the asteroid (115) Thyra. As discussed by Lehtinen et al. (2016), at radio wavelengths the shadow of the asteroid is often dominated by diffraction fringes. The observed diffraction pattern depends on the wavelength, and the size and the distance of the asteroid. A rule of thumb is that a sharp shadow is observed when the Fresnel number,  $F$ , is greater than 1, whereas a diffraction pattern in the Fraunhofer regime is observed for  $F \leq 1$  (e.g., Trahan & Hyland 2014). The Fresnel number is defined by  $F = a^2/(d\lambda)$ , where  $a$  and  $d$  are the radius and the distance of the occcluder, and  $\lambda$  is the wavelength.

Here we report on an asteroid occultation observation using the Very Long Baseline Array (VLBA; Napier et al. 1994), operated by the Long Baseline Observatory (LBO). The background source is the active galactic nucleus (AGN) 0141+268 (J0144+270), associated with a BL Lac type galaxy (Lister et al. 2016). At the wavelength used ( $\lambda = 4.2$  cm), the source consists of a compact nucleus,  $< 3$  milliarcseconds (mas), and a faint jet. An image of the source at 8.7 GHz from the VLBA experiment VCS-II-D/BG219D (June 9, 2014; Gordon et al. 2016), is shown in Figure 1.<sup>1</sup> The occcluder is the large main-belt asteroid (372) Palma. Recent estimates for its diameter from thermal modelling of mid-infrared photometric data range from 187 to 191 km (Carry 2012; Masiero et al. 2014).

The paper is organized as follows. In Section 2, we present the prediction for the occultation at Brewster, and in Section 3 we describe the VLBA observations. In Section 4, the observed visibilities are interpreted in terms of the Fresnel-Kirchhoff diffraction theory applied to different silhouette models. The results are discussed in Section 5.

## 2. OCCULTATION PREDICTION

Palma was predicted to occult the AGN 0141+268 (J0144+270) on May 15, 2017, as seen from the Brewster VLBA station (BR-VLBA). The predictions were made using the LinOccult program<sup>2</sup>. LinOccult requires three auxiliary data sets. 1) The position of the background object was adopted

<sup>1</sup> Other VLBA images and the radio spectrum of the source can be found at [www.physics.purdue.edu/MOJAVE](http://www.physics.purdue.edu/MOJAVE)

<sup>2</sup> <http://andyplekhanov.narod.ru/occult/occult.htm>

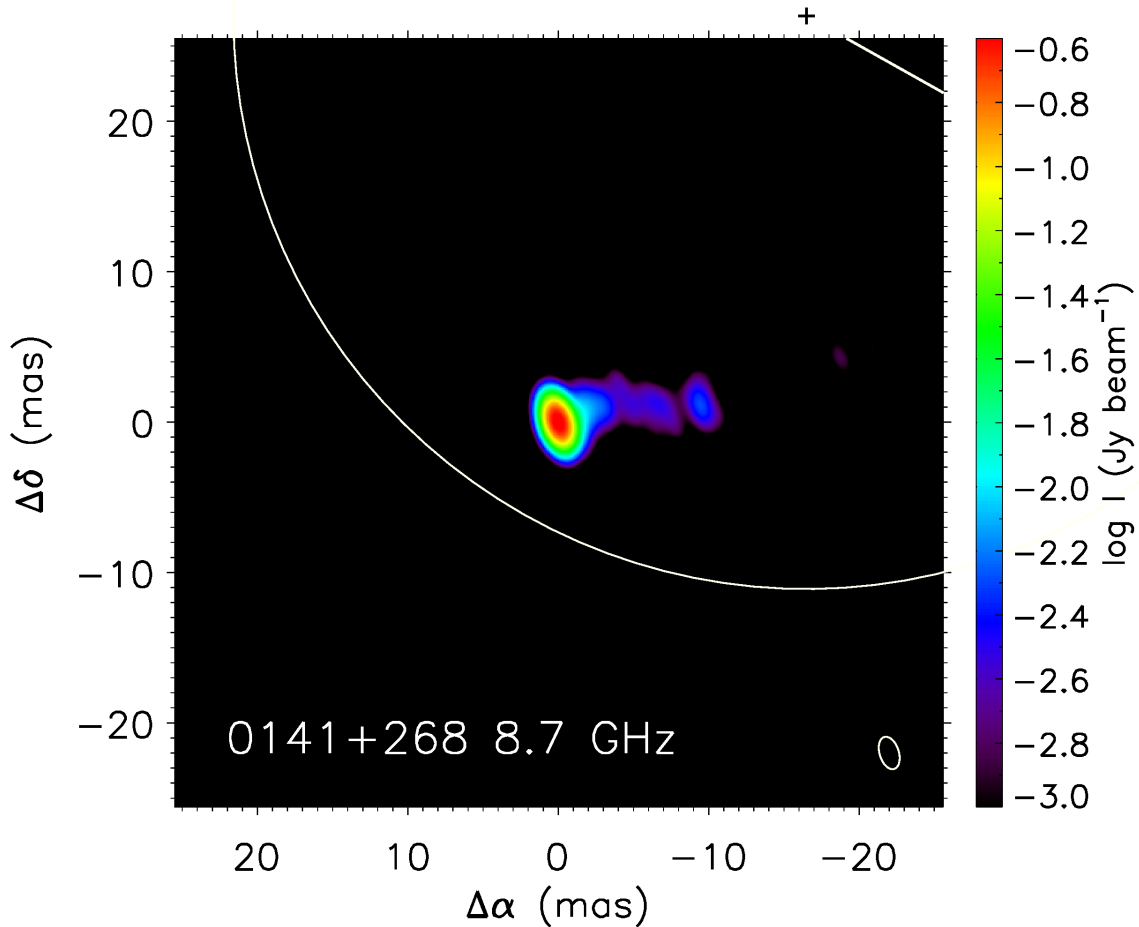


**Figure 1.** Image of the active galactic nucleus 0141+268 (J0144+270) at 8.7 GHz from the VLBA survey VCS-II (Gordon et al. 2016). The synthesized beam size of the observation is shown in the bottom right ( $2.2 \times 1.3$  mas, P.A.  $17.4^\circ$ ). The predicted closest position of (372) Palma as seen from Brewster is indicated with a plus sign (outside the frame). The white arc marks the approximate silhouette of the asteroid, assuming that it is a circular disk with a diameter of 190 km (76 mas).

from the latest Radio Fundamental Catalog (RFC), available at <http://astrogeo.org/rfc> (Petrov & Kovalev 2017; Petrov et al. 2008). 2) The orbital elements of the asteroid were taken from a database provided by Lowell Observatory<sup>3</sup>. 3) The ephemerides of the major planets were obtained using the JPL HORIZONS service<sup>4</sup>.

The asteroid radius ( $a \sim 95$  km; Carry 2012; Masiero et al. 2014), and its distance at the time of the observation ( $d \sim 3.436$  au) imply a Fresnel number of 0.43 at  $\lambda = 4.2$  cm. This means that a Fraunhofer diffraction pattern was observable on the Earth. The predicted shadow path in the vicinity of Brewster is shown in Figure 2. According to this prediction, the ground speed of the shadow was  $51 \text{ km s}^{-1}$  near Brewster, and the telescope was located just inside the geometric shadow at the time of the closest approach, UT 14:31:23. At this time, the asteroid and the radio galaxy were in the East, at an elevation of  $42^\circ$ . The projection of the shadow on the Earth is therefore elongated in an East-West direction. Also shown in this figure are the projections of the first bright ring of the

<sup>3</sup> <ftp://ftp.lowell.edu/pub/elgb/astorb.html>

<sup>4</sup> <ftp://ssd.jpl.nasa.gov/pub/eph/planets/Linux/de405>, file lnxp1600p2200.405

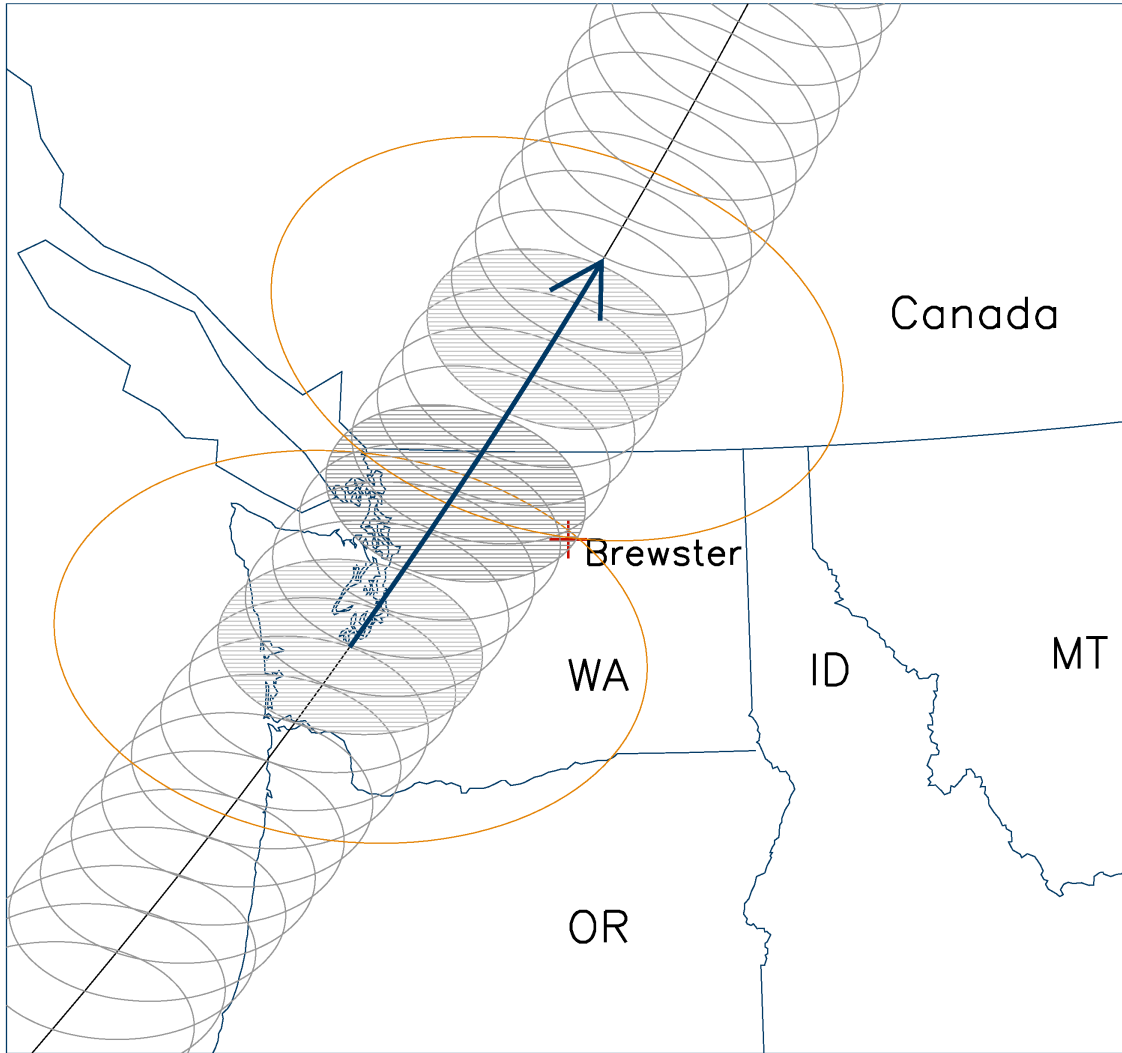


**Figure 2.** Shadow path of (372) Palma on May 15, 2017, near Brewster, Washington, United States. The arrow shows the distance the shadow traveled in ten seconds (510 km). The projections of the geometric shadow of the asteroid are shown with small ellipses at intervals of one second. The asteroid silhouette is approximated by a circular disk with a radius of 95 km. The two bigger ellipses show the first maxima of the diffracted intensity pattern outside the geometric shadow, 4 s before and after its closest approach to Brewster.

diffracted intensity pattern, 4 seconds before and after the deepest occultation. Detectable diffraction fringes extended to  $\sim 500$  km from the shadow center, signifying that other VLBA antennas than Brewster received unobscured signal from 0141+268.

### 3. VERY LONG BASELINE ARRAY OBSERVATIONS

The occultation was observed by six VLBA antennas: BR-VLBA (Brewster), FD-VLBA (Fort Davis), KP-VLBA (Kitt Peak), LA-VLBA (Los Alamos), PT-VLBA (Pie Town), and OV-VLBA (Owens Valley) located in the continental United States. The lengths of baselines to BR-VLBA ranged from 1.2 to 2.3 thousand kilometers. The central frequency of the observations was 6.996 GHz, and the total

bandwidth was 256 MHz. Both right and left circular polarizations were recorded with 2 bits per sample.

The observations started at UT 14:00, on May 15, with a five minute scan on the strong radio source 0149+218, which was used as the fringe finder and bandpass calibrator. Thereafter the antennas tracked 0141+268 until UT 15:00 with 10 s long pauses every 5 minutes. The occultation was predicted to be deepest at 14:31:23. System temperature ranged from 25 K to 35 K, and the System Equivalent Flux Density was in the range 240–290 Jy.

The data were correlated in the Science Operations Center in Socorro, using NRAO’s implementation of the DiFX (Distributed FX) software correlator (Deller et al. 2011; FX means that the Fourier transform is applied before the cross-multiplication of signals). The correlator integration time was 0.25 s and the frequency resolution was 250 kHz. Further processing was done with the *PTMA* VLBI data analysis software package<sup>5</sup>. The data were split into 290-s long segments, and the residual phase delay and group delays were fit into the spectrum of the cross-correlation function produced by the correlator, also known as the fringe visibility. Details of the fringe fitting procedure can be found in Petrov et al. (2011). The fringe visibilities were counter-rotated to the contribution of the group delay and the phase delay rate, and coherently averaged over frequency. Thereafter arithmetic averages over the five baselines were computed; the residual fringe phases were stacked with zero mean, and the stacked fringe amplitudes were normalized to unity.

The rms noise levels of the stacked amplitudes and phases over the 290 s interval including the occultation (excluding 20 s around the closest approach) are 0.079 and 0.083 rad, respectively. For individual baselines, the signal to noise ratio over this interval ranged from 184 to 224 with the mean 197. Assuming no losses in coherence, the expected rms of the normalized fringe amplitude and fringe phases is  $197 \cdot \sqrt{290/0.25/5} = 0.077$ , which is very close to the obtained values. In order to reduce the scatter in residual fringe amplitudes and phases, at the expense of the time resolution, we applied a weak Gaussian filter using the kernel  $\exp\{-(t - t_0)^2/(2a^2)\}$  with the parameter  $a = 0.35$  s.

Residual fringe phases exhibit fluctuations of  $\sim 0.1$  rad on time scales of 50–100 sec due to changes in the atmosphere path delay and possible phase and frequency offsets of the station clocks. In order to alleviate the contribution of these fluctuations, we fit a model to the fringe phases during the occultation. The model is defined by

$$M(p_1, p_2, t_0) = \begin{cases} p_1 \frac{\sin p_2(t - t_0)}{p_2(t - t_0)}, & t \in [t_0 - \frac{2\pi}{p_2}, t_0 + \frac{2\pi}{p_2}], \\ 0 & \text{otherwise} \end{cases}$$

After subtracting this model we applied a low-pass Gaussian filter with  $a = 10$  s to the residuals. Finally, we subtracted the smoothed, low-pass filtered phases from those filtered with  $a = 0.35$  s. These residual phases and amplitudes were used in the subsequent analysis. The rms scatter of this 270 s long dataset, with  $\pm 10$  s around the occultation excluded, is 0.033 for the normalized amplitude and 0.043 rad for the phase.

Only one antenna, BR-VLBA was affected by the occultation. During the occultation, the power of the signal recorded at BR-VLBA dropped, and the optical path delay from the source to the antenna changed with respect to the unobscured situation. The change in the path delay at BR-

<sup>5</sup> Documentation is available at <http://astrogeo.org/pima>

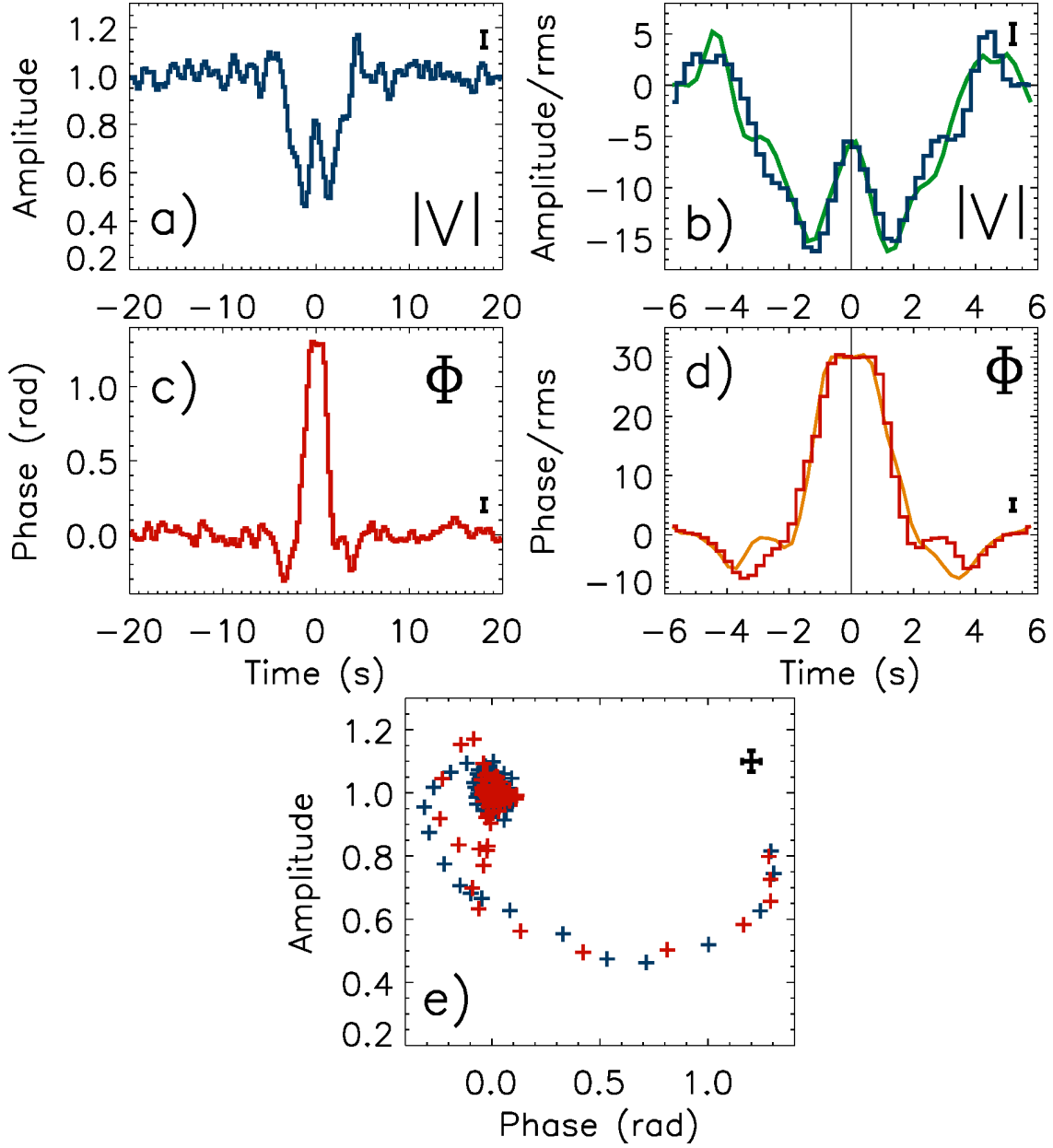


**Figure 3.** Stacked visibility amplitudes,  $\langle |V| \rangle$  (a), and phases,  $\langle \Phi \rangle$  (c), during the occultation. The averaging is performed over five VLBA baselines including Brewster. The time-series are smoothed to a resolution of 0.35 s. The amplitude of the unobscured signal is normalized to unity. The right panels (b and d) show 12 s portions of the amplitude and phase time-series in terms of the rms scatter. Time-inverted amplitude and phase curves (green and orange curves) are superposed to highlight asymmetries. The bottom panel (e) shows the amplitude vs. phase diagram. The points before and after the deepest occultation are indicated with blue and red, respectively.

VLBA propagates directly to the visibility phases,  $\Phi$ , for all the five baselines including Brewster. In contrast, the change in the normalized visibility amplitude,  $|V|$ , during the occultation is proportional to the square root of the relative power drop measured at BR-VLBA, that is,  $|V| \propto \sqrt{\frac{\Delta P_B}{P_B}}$ .

The stacked and smoothed residual amplitudes and phases are shown in Figure 3 (panels a and c). A zoomed-in view of the time-series, normalized to the rms scatter, is presented on the right of this figure (panels b and d). In panel b, the zero level corresponds to the average normalized amplitude of the unobscured signal. Also shown in panels b and c are the amplitudes and phases with the time axis reversed. This is to highlight asymmetries between the immersion and emergence sides. The intensity minima caused by the obscuration of the background source, and the Arago-Poisson spot between these minima are detected at levels exceeding  $10\sigma$  in the amplitude curve. The maximum phase shift associated with the deepest occultation is 1.3 radians ( $\sim 30\sigma$ ). The amplitude maxima on both sides of the deep minima, corresponding to the first intensity maxima of the diffraction pattern, are detected at levels of  $3\sigma$  (immersion) and  $5\sigma$  (emergence). The depths of the phase minima occurring at the same time, are approximately  $8\sigma$  (immersion) and  $6\sigma$  (emergence). The shapes of the amplitude bumps and the phase dips are different on the immersion and emergence sides, the difference being more prominent in the phase curve. The difference is also visible in the amplitude versus phase plot shown in panel e of Figure 3. In this diagram, the center of the occultation curve, with the maximum phase shift lies on the right, and the unobscured baselines before and after the occultation correspond to the concentration of points around phase 0, amplitude 1. The visibilities on the immersion and emergence sides of the occultation are plotted with blue and red symbols, respectively.

## 4. PREDICTED VISIBILITIES FROM SILHOUETTE MODELLING

### 4.1. Circular disk

We first model the occultation curves assuming that the occluder is a circular disk. The background radiation source, the radio galaxy 0141+268, is dominated by a point source, and the incident wavefront can be taken to be planar. The formula for the complex diffracted amplitude applicable to this case are given, for example, by [Roques et al. \(1987\)](#) (Eqs. B2 and B4 in their Appendix B) and by [Aime et al. \(2013\)](#) (their Sect. 5.3).

The three input parameters of the circular disk model are the asteroid radius,  $a$ , the perpendicular distance,  $\Delta$ , of Brewster from the center of the shadow path, and the time,  $t_0$ , of the closest approach. The set of input parameters producing the closest match to the observed visibility amplitudes and phases were determined by finding the minimum of a reduced  $\chi^2$  function. We compare both amplitudes and phases to the model predictions, and define the  $\chi^2$  function by

$$\chi^2 = \frac{1}{n-p} \sum_{i=1}^n \left( \frac{|V|_i^{\text{obs}} - |V|_i^{\text{calc}}}{\sigma_i^{|V|}} \right)^2 + \frac{1}{n-p} \sum_{i=1}^n \left( \frac{\Phi_i^{\text{obs}} - \Phi_i^{\text{calc}}}{\sigma_i^{\Phi}} \right)^2, \quad (1)$$

where  $n$  is the number of the data points,  $p$  is the number of free parameters (here 3),  $|V|_i$  is the visibility amplitude, and  $\Phi_i$  is the visibility phase. The superscripts “obs” and “calc” refer to the observed and calculated values, respectively.

The values of the radius, and the distance and time of the closest approach found by this minimization are  $a = 95.9 \pm 2.4$  km,  $\Delta = -31.6 \pm 3.4$  km, and  $t_0 = \text{UTC } 14:31:19.63 \pm 0.07$  s (Coordinated Universal Time). The predicted diffracted intensity and phase patterns for a circular obstacle with the quoted radius are shown in Figure 4 (panels b and c). The predicted visibility amplitudes and phases at the best-fit perpendicular distance from the shadow centre are shown below them (panels

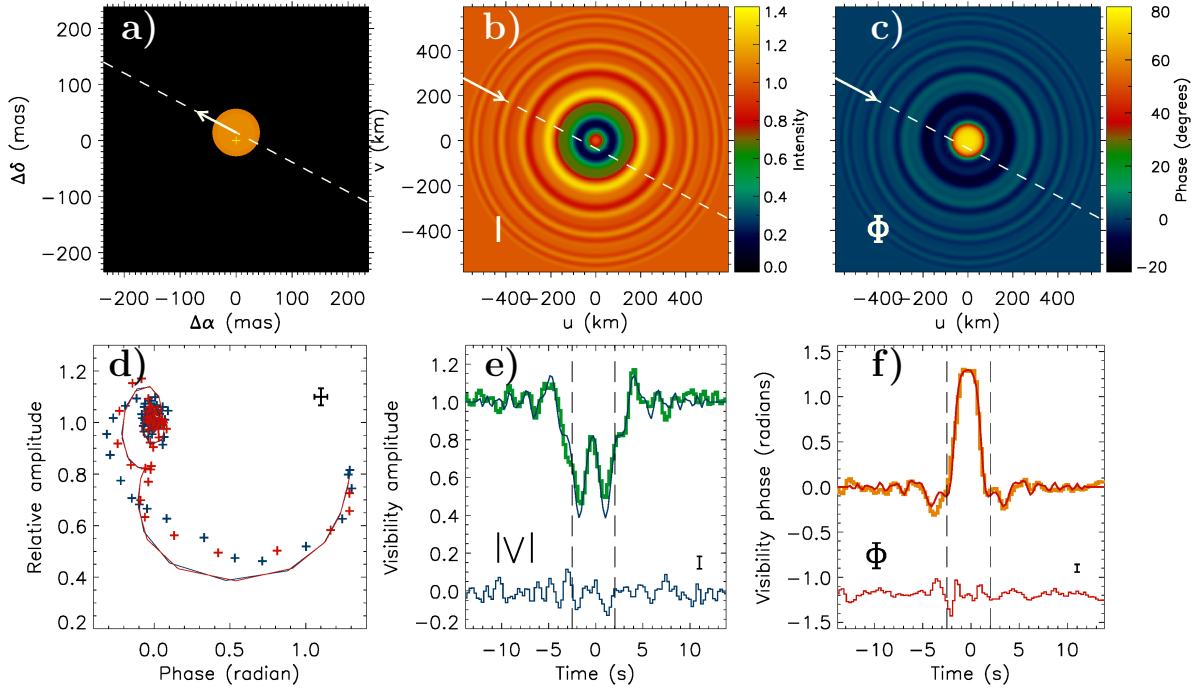


**Figure 4.** Top: Opaque circular disk (a) and the intensity (b) and phase (c) patterns of a plane wave diffracted by this obstacle. The radius of the occluder and its shortest projected distance from the background source (plus sign) are adjusted to agree with the occultation curves produced by Palma. The silhouette is drawn on the celestial sphere, whereas the diffraction patterns are projections onto a plane perpendicular to the direction of the radiation source. The dashed line in panel a shows the path of the asteroid in the sky relative to the background source. The dashed lines in panels b and c indicate the cross-section of the diffraction pattern measured at Brewster. Bottom: Visibility amplitude versus phase (d) and the amplitude (e) and phase (f) profiles along the dashed lines shown in the top. In panel d, the observing points corresponding to the immersion and the emergence are indicated with blue and red, respectively. In the calculated diagram, these two sides overlap perfectly, because the obstacle is symmetric. The observed time-series of the visibility amplitudes and phases during the occultation of Palma are shown with thick green and orange lines. The time range ( $\sim 30$  s) corresponds to the spatial range ( $\sim 1200$  km) of the images. The residuals after subtracting the model from the observations are shown in the bottom of panels e and f.

e and f), together with the observed amplitudes and phases. The corresponding amplitude vs. phase diagrams are shown in panel d of this figure.

#### 4.2. Polyhedral models from lightcurves

Two polyhedral models for Palma, with different spin axis ecliptic coordinates ( $\lambda_P, \beta_P$ ) are available via an interactive service provided by Astronomical Observatory, Poznań (Marciniak et al. 2012)<sup>6</sup>. The models are derived from photometric observations using lightcurve inversion (Kaasalainen et al. 2001; Āurech et al. 2011; Hanuš et al. 2011). The predicted silhouettes of Palma at the time of the occultation were used to calculate intensity and phase maps. The silhouette prediction takes into account the light travel time (approximately 28.5 minutes). The rotation period of Palma is 8.6 hours.

<sup>6</sup> isam.astro.amu.edu.pl

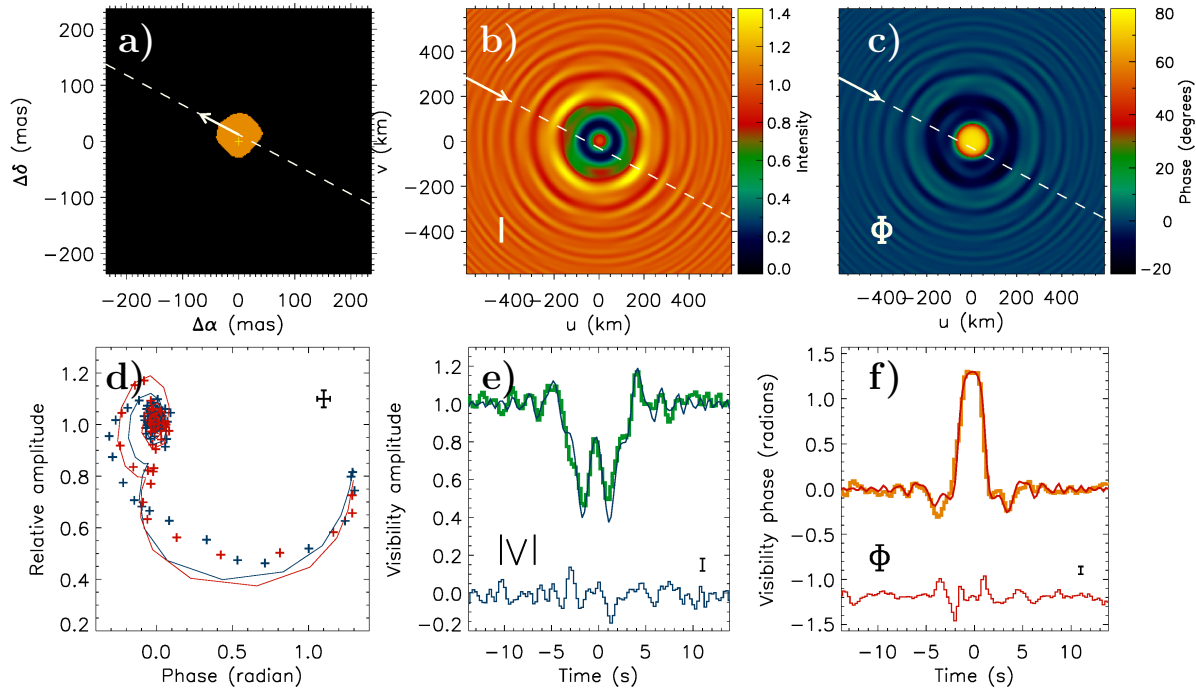


**Figure 5.** Same as Figure 4 but the silhouette model is adopted from the Interactive Service for Asteroid Models (ISAM). The model is based on lightcurve inversion of photometric observations (see text).

The diffraction patterns were calculated using a method adopted from Trahan & Hyland (2014). In this method, the silhouette is presented as a grid of rectangles, and the complex amplitude of the diffracted wavefront is obtained as the sum of those caused by individual rectangles. The resulting complex amplitude is given in Eq. (10) of Trahan & Hyland (2014) (inside the modulus bars).

The polyhedral models are given in the celestial coordinate system. These models are asymmetric, and the angle at which the asteroid crossed the radio source affects the occultation curve. The apparent motion of the asteroid in the sky relative to the radio source was directed from the southwest to the northeast; the tilt angle with respect to the hour circle passing through the radio source was approximately  $62^\circ$  ( $152^\circ$  measured counterclockwise from the declination circle). The orientation of the measured cross-section of the diffraction pattern was also indicated for the circular disk model (Figure 4), although for a symmetric occcluder the obliqueness is of no consequence. The tilt angle is determined by the orientation of the ecliptic and the inclination of the asteroid orbit with respect to this. Because the inclination is assumed to be known to a high accuracy, the tilt angle is kept constant in the present calculations.

We fitted the observed occultation curves with the shapes from lightcurve inversion by varying the effective radius of the model, and the distance and the time of the closest approach. The effective radius is defined by  $a_{\text{eff}} = \sqrt{A/\pi}$ , where  $A$  is the projected area of the asteroid. The diffraction patterns and the predicted occultation curves for one of the asteroid models (with the spin vector ecliptic coordinates  $\lambda_P = 221^\circ$ ,  $\beta_P = -47^\circ$ ; we call this model 1) are shown in Figure 5. The best-fit parameters of this model are  $a_{\text{eff}} = 95.8 \pm 2.7$  km,  $\Delta = -26.1 \pm 3.9$  km, and  $t_0 = \text{UTC } 14:31:19.66 \pm 0.07$  s. The other model (“model 2”), with  $\lambda_P = 44^\circ$ ,  $\beta_P = 17^\circ$ , gives similar best-fit parameters, but with larger residuals. Model 2 is clearly elongated in a North-South direction at the time of

**Table 1.** Best-fit parameters of silhouette models

Model	$a_{\text{eff}}$ (km)	$\Delta$ (km)	$t_0$ UTC 14:31 +	Other parameters	$\chi^2_\nu$
circle	$95.9 \pm 2.4$	$31.6 \pm 3.4$	$19.63 \pm 0.07$ s		3.76
polyhedral model 1	$95.8 \pm 2.7$	$26.1 \pm 3.9$	$19.66 \pm 0.07$ s		4.61
polyhedral model 2	$97.2 \pm 2.1$	$34.7 \pm 2.7$	$19.57 \pm 0.07$ s		6.01
ellipse	$96.1 \pm 2.4$	$25.4 \pm 4.5$	$19.68 \pm 0.07$ s	$e = 0.40 \pm 0.13$ , $\Phi = -3.1^\circ \pm 16.3^\circ$	3.59
binary	$95.5 \pm 2.4$	$18.8 \pm 3.8$	$19.41 \pm 0.12$ s	$a_2/a_1 = 0.63 \pm 0.06^a$ , $\Phi = -21^\circ \pm 7^\circ$ , $s = 0.7 \pm 0.1^b$	6.41
curved	$95.5 \pm 2.2$	$2.1 \pm 3.8$	$19.92 \pm 0.12$ s	$a_2/a_1 = 0.60 \pm 0.07^a$ , $\Phi = -92^\circ \pm 6^\circ$ , $s = 1.2 \pm 0.1^b$	6.00

<sup>a</sup>  $a_2/a_1$  is the ratio of the radii of the two circles forming the shape. <sup>b</sup>  $s$  is the distance of the two circles divided by  $a_{\text{eff}}$ .

the occultation. The fit parameters of the two polyhedral models and all the geometrical shapes considered in the present work are listed in Table 1.

Compared with the circular disk model, the polyhedral models do not improve the overall agreement between the observed and predicted amplitude and phase curves. Model 1 reproduces reasonably well the amplitude maximum on the emergence side (corresponding to the arch of red plus signs in the top left of the amplitude vs. phase diagram), but neither of the models can reproduce the prominent dent in the phase on the immersion side (the bight of blue crosses on the left). Both the circular disk and the adopted polyhedral models produce overly deep amplitude minima on both sides of the Arago-Poisson spot. In the amplitude vs. phase diagram, the effect is that the predicted curves lie below the observed points in the middle of the plot (between phases 0 and 1 radian).

#### 4.3. Other shapes: elliptical, potato-shaped and curved models

The models tested above fail to reproduce some conspicuous features of the amplitude and phase curves. Therefore, we tested the effects of elongation and asymmetry using elliptical, potato-shaped, and concave silhouettes. The parameters of the elliptical models are the effective radius,  $a_{\text{eff}}$ , the eccentricity,  $e$  (varied between 0.1 and 0.9), and the orientation angle,  $\Phi$ , of the major axis (measured counterclockwise from the declination circle).

The potato-like binary model is composed of two partly overlapping circular disks with radii  $a_1$  and  $a_2$ . The parameters of this model are the effective radius,  $a_{\text{eff}}$ , the ratio  $a_2/a_1$  of the radii of the two disks (varied in the range  $0.3 \rightarrow 1$ ), the separation between the disks (varied between  $a_1 - a_2$  and  $a_1 + a_2$ ), and the orientation of the axis connecting the circles. In the curved model, one edge of the otherwise convex silhouette is hollow. The model is realized in the same manner as the potato-shaped binary, except that the secondary circle is empty.

In all models, the perpendicular distance of the observing site from the center of the shadow path, and the time of closest approach are free parameters. The tilt angle of the cross-section measured at Brewster was kept constant ( $152^\circ$  from the declination circle) like in the previous models.

The best-fit parameters of the mentioned geometrical shapes, together with those of the circular disk and polyhedral models discussed above, are presented in Table 1. The best-fit elliptical, potato-like binary, and curved silhouette models are shown in Appendix A, in Figures 9, 10, Figure 11, respectively. For all shapes considered here, the best-fit effective radius is  $a_{\text{eff}} \sim 96$  km. For elongated models, the long axis lies approximately east-west. The elliptical model gives the smallest chi-square values of all the models tested here.

In the best-fit potato-shaped binary model, the “secondary” is a protrusion of the “primary” disk on the trailing side of the asteroid. The situation where the kink in the amplitude vs. phase diagram is only seen at emergence (red plus signs in the amplitude vs. phase diagram) can be realized with this model. However, judging from the  $\chi^2$  analysis, the binary model is in worse agreement with the observed occultation curves than the elliptical and circular disks and the polyhedral model 1. Furthermore, neither this nor any other of the convex models can generate the deep phase minimum on the immersion side (the arch of blue plus signs with negative phases).

In the best-fit curved model the southern edge of the silhouette was hollow during the occultation. Occultation curves produced by this model agree reasonably well with the observations on the immersion side, and can reproduce the kink on the emergence side of the amplitude vs. phase diagram. However, the overall agreement with the observed occultation curves (in terms of  $\chi^2$ ) is worse than with the other models discussed here, albeit comparable with that of the polyhedral model 2. In particular, the concave model overestimates the strength of the Arago-Poisson spot. The spot can be made weaker by increasing the distance of the closest approach, but this would worsen the agreement at the amplitude minima.

#### 4.4. Estimate of the roundness

Shapes obtained from lightcurve inversion and the present efforts to model the radio occultation curves suggest that the asteroid silhouette deviates from a perfect circle. When the roundness of the shape is characterized by the ratio,  $r$ , of the inscribed and circumscribed circles, the roundness of the best-fit polyhedral model is  $r = 0.83$ , whereas for the best-fit elliptical model ( $e = 0.4$ ) this ratio is  $r = 0.92$ . As no one of the simple geometrical shapes nor the polyhedral model could satisfactorily reproduce the observed occultation curves, we estimate the roundness by generating a sequence of random contiguous silhouettes using the Metropolis-Hastings algorithm. The distribution of the roundness parameter of random silhouettes obtained in this manner should approximate the probability distribution of the roundness of Palma.

In the silhouette models we only varied the ratio of the minimum and maximum circles that just fit inside and enclose the shape, but kept the effective radius, that is, the surface area of the asteroid, constant. We used the best-fit value,  $a_{\text{eff}} = 96$  km, from the simulations described above. In each step of the sequence, the roundness parameter  $r'$  was picked at random from a Gaussian distribution centered on the previously accepted value  $r$ . The area inside minimum radius was then completely filled, and the area between the minimum and maximum radii was filled with randomly placed pixels, however so that the result was contiguous.

The  $\chi^2$  value of the best-fit cross-section of the diffraction pattern was used as measure of the probability of the model,  $\ln P(r) \propto -0.5 \chi^2$ , and in accordance with the Metropolis-Hastings principle, the acceptance ratio,  $\ln P(r') - \ln P(r)$ , was compared with the logarithm of a uniform random number on the interval  $[0, 1]$  when deciding whether to accept or reject the candidate  $r'$ . The roundness distribution of 24,000 realizations of random shapes constructed in the course of this procedure is

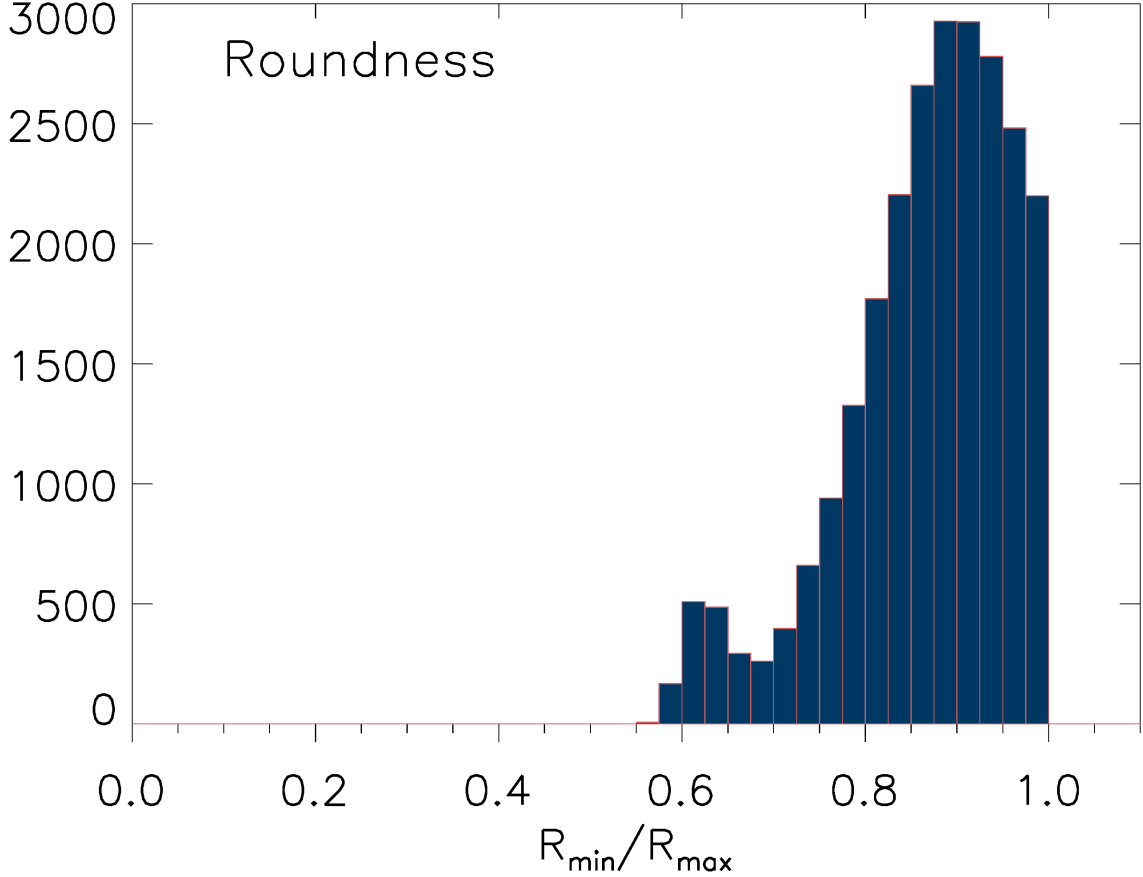


**Figure 6.** Distribution of the ratio of the inscribed and circumscribed radii for a sample of 24,000 contiguously random shapes, constructed by a Markov chain Monte Carlo method described in the text. The histogram is assumed to correspond to the probability distribution of the roundness parameter of the models explaining the amplitude and phase curves observed during the radio occultation by Palma.

shown in Figure 6. The distribution is skewed to the left because  $r$  cannot exceed unity. The moments of the distribution are  $\mu_r = 0.866$  (mean),  $\sigma_r = 0.093$  (standard deviation), and  $\gamma_1 = -0.952$  (skewness). The distribution suggests that the asteroid shape deviates from a perfect circle by 10–20%. The roundness parameter is greater than 0.63 with 95 percent confidence. One of the random models giving a reasonably good agreement with the occultation curves is shown in Figure 12 of Appendix A.

## 5. DISCUSSION

### 5.1. Angular resolution of the observation

The occultation measurement described here is performed by keeping the radiation source near the optical axis of the antenna, and the detectable diffraction pattern, that is, a few first maxima and minima, are observed in the region where the normalized beam pattern is unity. The effect of the finite beamwidth of the antennas (depending on the angle subtended by the antenna seen from the asteroid) is negligible. The resolution at which the diffraction fringes are observed are therefore primarily determined by the sampling rate permitted by the noise level, the speed of the shadow on Earth ( $19.25 \text{ mas s}^{-1}$  in the sky; the ground speed is  $51 \text{ km s}^{-1}$ ), and the bandwidth

smearing (chromatic aberration) caused by the averaging of the frequency channels over the receiver bandwidth. Both the sampling rate and the need of averaging spectral channels depend on the signal-to-noise ratios in the occultation curves, which therefore determine how accurately the observed fringe patterns can be modeled or inverted. The correlator integration period, 0.25 seconds, translates to an angular resolution of approximately 5 mas. We think that in the case of Palma observations we could have used a shorter averaging interval which would have resulted in a more accurate determination of the occultation time.

The finite size of the background source can give rise to yet another smoothing effect (Roques et al. 2008). In the present observations this effect is, however, negligible; 99% of the flux comes within an angular radius of  $\sim 3$  mas, which is much smaller than the angular Fresnel scale,  $\sqrt{\lambda/2d} \sim 40$  mas. For this estimate we reprocessed VCS-II/BG219D VLBA segment observed on June 9, 2014 (Gordon et al. 2016), and produced the 8.7 GHz image of 0141+268 shown in Figure 1. To examine the magnitude of this smoothing effect, we calculated the amplitude and phase curves from a circular occcluder using the actual radio map, and found no visible difference from the calculation which used a point source (as in the examples presented above). For basic principles and methods of radio (lunar) occultation measurements we refer the reader to Hazard (1976).

### 5.2. Size and shape of the asteroid

The possibility of measuring both the amplitude and the phase of the diffracted wavefront increases significantly the accuracy of asteroid sizing as compared with single-dish observations. The maximum phase shift is particularly sensitive to the effective diameter of the asteroid. This can be seen in Figure 7 which shows the maximum and minimum amplitude and phase of wavefront diffracted by a circular obstacle as functions of the Fresnel number,  $F$ . The phase shift is directly proportional to  $F$  with the proportionality constant  $\pi$ . The minimum and maximum curves in Figure 7 represent measurements through the shadow's center, whereas the observed cross-section of the diffraction pattern is off from the center. Because the phase pattern is flat topped (see Figure 4), a small offset does not affect the maximum phase. In contrast, the Arago-Poisson spot is strongly peaked, and the strength of the central maximum decreases rapidly with the distance from the shadow center. All silhouette models considered here give practically the same best-fit effective diameter for Palma. This diameter,  $192.1 \pm 2.3$  km, corresponding to the maximum phase shift  $76.4^\circ \pm 2.5^\circ$ , agrees very well with recent determinations from thermal emission at infrared wavelengths (Carr 2012:  $191.1 \pm 2.7$  km; Masiero et al. 2014:  $186.5 \pm 6.3$  km).

Even though the exact shape of the occcluder is difficult to discern in Fraunhofer diffraction, deviations from circular shape can leave recognizable traces to the occultation curves. The amplitude and phase curves observed here are better reproduced by an elliptical silhouette than by a circular screen with the same projected area (Figures 4 and 9). The amplitude vs. phase plot is useful for identifying asymmetries. Characteristic of the diagram derived from the present observations is a kink seen only on the emergence side, and a prominent depression of phases on the immersion side. The kink can be brought about by a protrusion on the trailing edge of the silhouette, whereas the phase minimum can be generated by a hollow edge. However, the elliptical and circular disks and one of the polyhedral models from lightcurves (model 1) give better overall agreement with the data than these asymmetric models. On the other hand, no one of the simple geometrical shapes considered here can satisfactorily explain the observed signal. For acceptable models, the reduced chi-square divided by the degrees of freedom as defined in Eq. 1 should be less than 2.5, whereas the minimum value listed

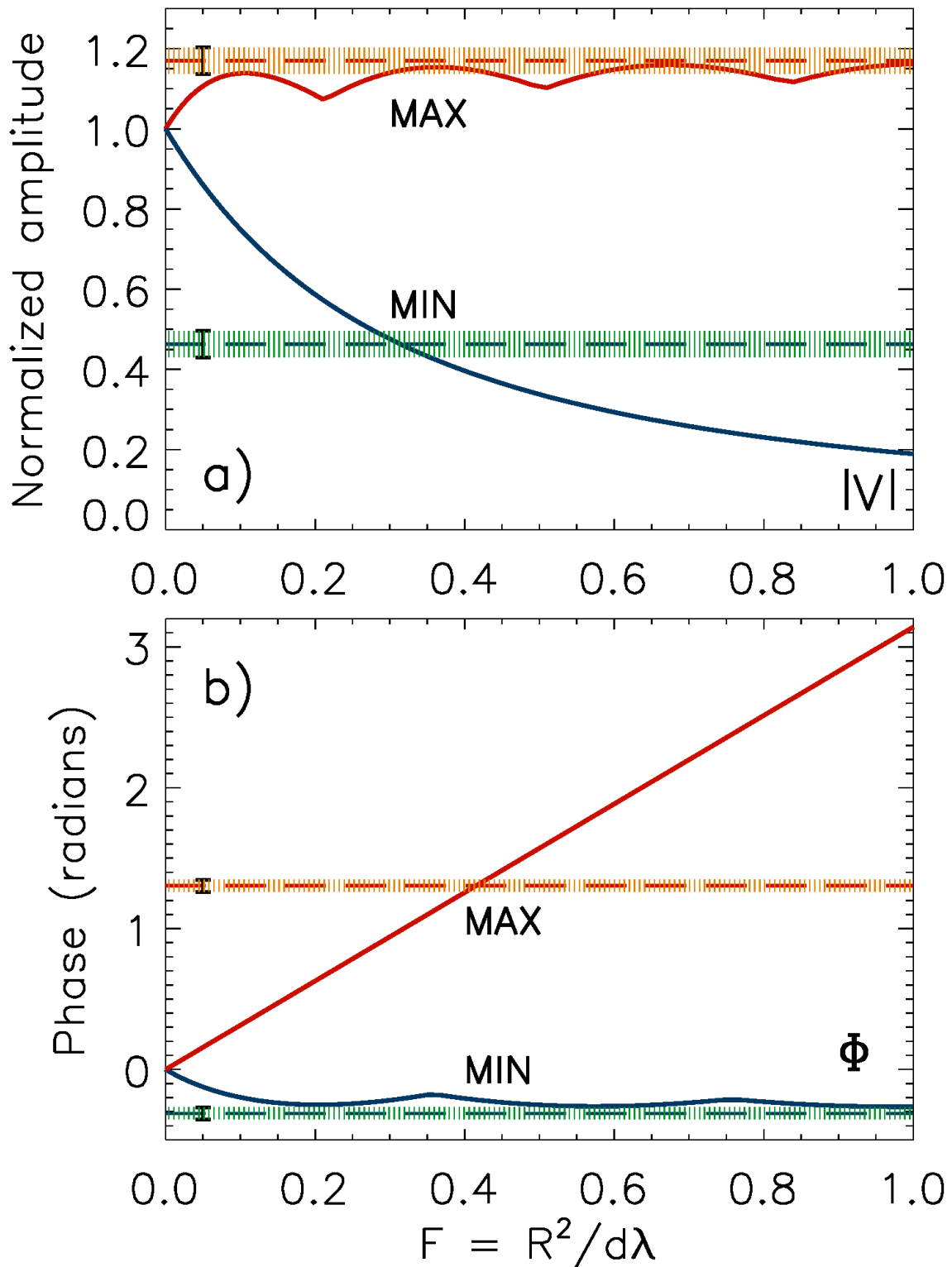


**Figure 7.** Maximum and minimum amplitude (a) and phase shift (b) of the diffracted wavefront as functions of the Fresnel number,  $F = R^2/(d\lambda)$ , for a circular disk with the radius  $R$ . The other parameters here are the distance,  $d$ , and the wavelength,  $\lambda$ . The hatched horizontal bars describe the observed maximum and minimum values and their  $1\sigma$  errors.

in Table 1 is 3.6 (see, e.g., Lampton et al. 1976). It seems possible to find a good solution for the asteroid shape by a combination of the models discussed above. Several random shapes generated in the course the Markov chain Monte Carlo sequence discussed in Section 4.4 give acceptable fits to the occultation curves. One example is shown in Figure 12. These random shapes are, however, too irregular to offer a plausible model for a 200-km diameter asteroid with substantial surface gravity.

One could try the technique of pixel by pixel reconstruction described by Trahan & Hyland (2014), together with constraints on the smoothness of the surface. However, a single cut through the diffraction pattern is generally insufficient for providing a unique solution. According to Trahan & Hyland (2014) it is possible to reconstruct the shape of an occcluder with several measurements of the intensity profile through the shadow pattern. They estimate that an unambiguous recovery of the silhouette requires twice as many measurement points (number of apertures times number of samples per aperture) than there are pixels in the silhouette image. The silhouette models used here have approximately 300 pixels, while the total number of useful measurement points (in amplitude and phase) is  $\sim 160$ . Besides requirements on the number of measurements and the noise level, the measurements should cover different parts of the diffraction pattern to provide for a unique solution for the asteroid shape. The spacing between telescopes across the shadow path should be of the order of the spatial Fresnel scale,  $\sqrt{d\lambda}/2$ , which in the case of Palma is  $\sim 100$  km. Currently such spacings would be available with VLBI networks, such as the VLBA and its counterparts in other continents, in the fortuitous event that the shadow of an asteroid should pass over two or more of their antennas.

### 5.3. Implications to the asteroid orbit

The measurement of the occultation curves in the Fraunhofer regime gives an estimate for the position of the asteroid at the time of the deepest occultation. Especially when the Arago-Poisson spot is detected, the time of closest approach, and the positional offset between the radio source and the center of the asteroid at that time can be determined rather accurately.

The measured apparent coordinates for Palma on 2017-05-15 14:31:19.68 UTC as seen from BR-VLBA are RA 01:44:33.5535 and Dec 27:05:03.127. Both coordinates have an uncertainty of 0.002", mostly due to uncertainties in the topocentric distance to Palma and the timing of the closest encounter ( $\Delta t_0 = 0.07$  s). The position of 0141+268 is known with an order of magnitude higher accuracy; according to the Radio Fundamental Catalog (RFC) the uncertainties of the RA and Dec coordinates are 0.21 mas and 0.28 mas, respectively. The ephemeris by the Jet Propulsion Laboratory's HORIZONS system for the observing date is in agreement with the measurement given a  $3\sigma$  ephemeris uncertainty of about 0.05". Including the coordinates derived from the radio occultation should reduce the uncertainty of the orbital solution given that the ephemeris uncertainty is an order of magnitude larger than the measurement uncertainty. To test this hypothesis we computed an orbital solution for Palma with all existing optical astrometry and the radio occultation included using the OpenOrb software (Granvik et al. 2009). We used the linearized least-squares method with outlier rejection and included gravitational perturbations by all eight planets and the 25 most massive asteroids as well as first-order relativistic corrections for effects caused by the Sun. For observational error model we use that by Baer et al. without correlations (Baer et al. 2011; Baer & Chesley 2017). Although the more than 1,600 astrometric observations of Palma span more than 120 years (1893-09-29 to 2017-11-09), the addition of a single radio occultation measurement has a non-negligible effect on the uncertainties of the orbital elements (typically tens of percent) and reduces the uncertainty of ephemerides by an order of magnitude (Figure 8).

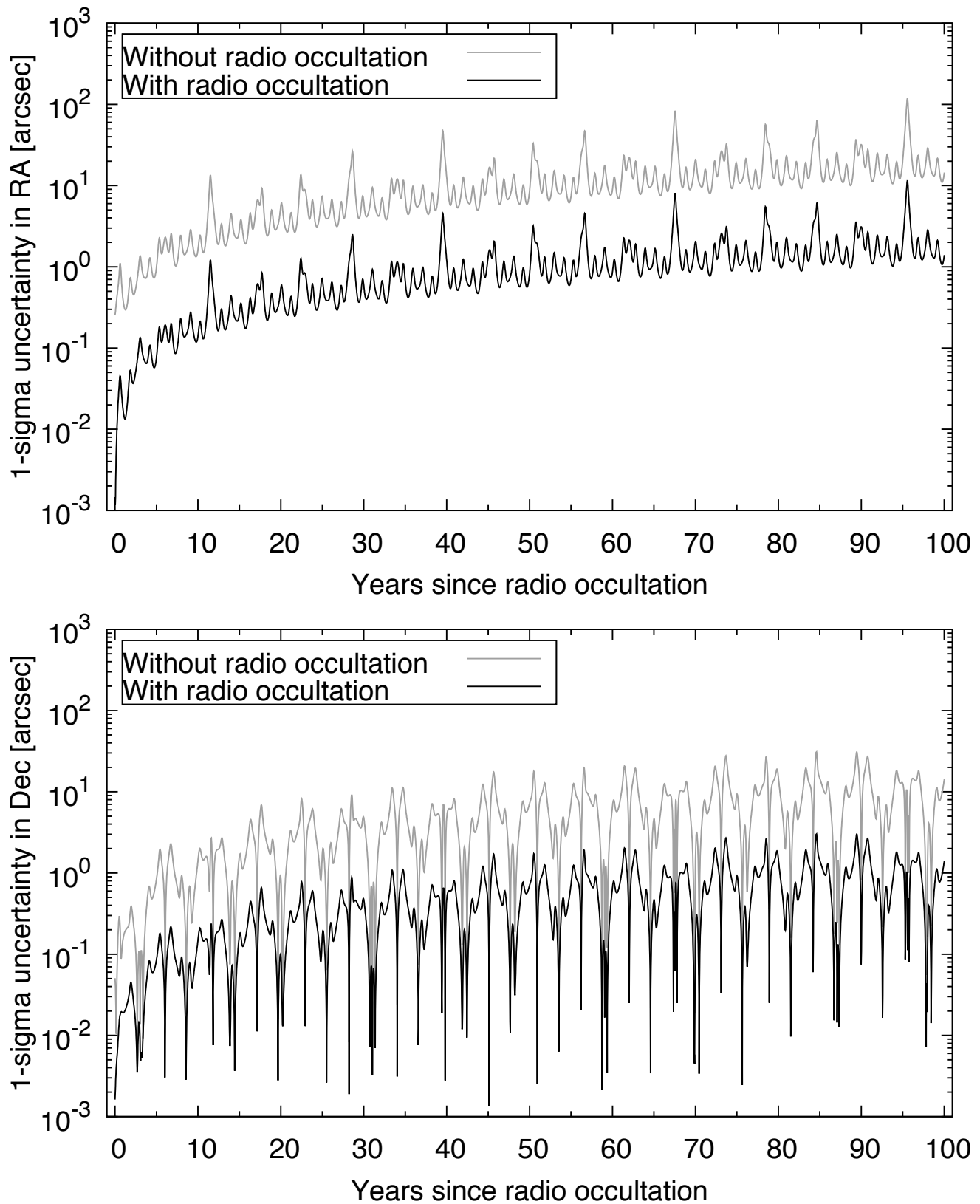


**Figure 8.** Ephemeris uncertainty for (372) Palma for 100 years the occultation in (top) RA and (bottom) Dec for a hypothetical geocentric observer. The black line refers to the prediction which includes the occultation-based astrometry whereas the gray line is a reference which does not include information about the occultation. The long-term trend in the ephemeris uncertainty is caused by the increasing orbital uncertainty and the short-term fluctuation is caused by the varying distance from the Earth to the asteroid (the peaks correspond to shortest distances).

The National Radio Astronomy Observatory is a facility of the National Science Foundation operated under cooperative agreement by Associated Universities, Inc. This work made use of the Swinburne University of Technology software correlator, developed as part of the Australian Major National Research Facilities Programme and operated under licence. J.H. and K.M. acknowledge support from the ERC Advanced Grant No. 320773 'SAEMPL'. M.G. acknowledges support from the Academy of Finland (grant #299543). We thank helpful discussions with Mika Juvela.

## REFERENCES

- Aime, C., Aristidi, É., & Rabbia, Y. 2013, in *EAS Publications Series*, Vol. 59, *EAS Publications Series*, ed. D. Mary, C. Theys, & C. Aime, 37–58
- Baer, J., & Chesley, S. R. 2017, *AJ*, 154, 76
- Baer, J., Chesley, S. R., & Milani, A. 2011, *Icarus*, 212, 438
- Carry, B. 2012, *Planet. Space Sci.*, 73, 98
- Cernicharo, J., Brunswig, W., Paubert, G., & Liechti, S. 1994, *ApJL*, 423, L143
- Deller, A. T., Brisken, W. F., Phillips, C. J., et al. 2011, *PASP*, 123, 275
- Gordon, D., Jacobs, C., Beasley, A., et al. 2016, *AJ*, 151, 154
- Granvik, M., Virtanen, J., Oszkiewicz, D., & Muinonen, K. 2009, *Meteoritics and Planetary Science*, 44, 1853
- Hanuš, J., Ďurech, J., Brož, M., et al. 2011, *A&A*, 530, A134
- Hazard, C. 1976, in *Methods of Experimental Physics*, Vol. 12 C, *Astrophysics. Radio Observations*, ed. M. L. Meeks, 92
- Hazard, C., Gulkis, S., & Bray, A. D. 1967, *ApJ*, 148, 669
- Hazard, C., Mackey, M. B., & Shimmins, A. J. 1963, *Nature*, 197, 1037
- Kaasalainen, M., Torppa, J., & Muinonen, K. 2001, *Icarus*, 153, 37
- Kooi, J. E., Fischer, P. D., Buffo, J. J., & Spangler, S. R. 2017, *SoPh*, 292, 56
- Lampton, M., Margon, B., & Bowyer, S. 1976, *ApJ*, 208, 177
- Lehtinen, K., Bach, U., Muinonen, K., Poutanen, M., & Petrov, L. 2016, *ApJL*, 822, L21
- Lister, M. L., Aller, M. F., Aller, H. D., et al. 2016, *AJ*, 152, 12
- Maloney, F. P., & Gottesman, S. T. 1979, *ApJ*, 234, 485
- Marciniak, A., Bartczak, P., Santana-Ros, T., et al. 2012, *A&A*, 545, A131
- Masiero, J. R., Grav, T., Mainzer, A. K., et al. 2014, *ApJ*, 791, 121
- Napier, P. J., Bagri, D. S., Clark, B. G., et al. 1994, *IEEE Proceedings*, 82, 658
- Oke, J. B. 1963, *Nature*, 197, 1040
- Petrov, L., & Kovalev, Y. Y. 2017, *MNRAS*, 467, L71
- Petrov, L., Kovalev, Y. Y., Fomalont, E. B., & Gordon, D. 2008, *AJ*, 136, 580
- . 2011, *AJ*, 142, 35
- Roques, F., Georjevits, G., & Doressoundiram, A. 2008, *The Kuiper Belt Explored by Serendipitous Stellar Occultations*, ed. M. A. Barucci, H. Boehnhardt, D. P. Cruikshank, A. Morbidelli, & R. Dotson, 545–556
- Roques, F., Moncuquet, M., & Sicardy, B. 1987, *AJ*, 93, 1549
- Scheuer, P. A. G. 1962, *Australian Journal of Physics*, 15, 333
- Schloerb, F. P., & Scoville, N. Z. 1980, *ApJL*, 235, L33
- Schmidt, M. 1963, *Nature*, 197, 1040
- Trahan, R., & Hyland, D. 2014, *ApOpt*, 53, 3540
- Ďurech, J., Kaasalainen, M., Herald, D., et al. 2011, *Icarus*, 214, 652
- von Hoerner, S. 1964, *ApJ*, 140, 65
- Withers, P., & Vogt, M. F. 2017, *ApJ*, 836, 114

## APPENDIX

## A. DIFFRACTION PATTERNS AND OCCULTATION CURVES FROM SOME GEOMETRICAL SHAPES AND A CONTIGUOUSLY RANDOM SHAPE

The best-fit elliptical, potato-like binary, and curved models for Palma described in Section 4.3, and the corresponding diffraction patterns and occultation curves are shown in Figures 9, 10, and 11. Figure 12 shows an example of a random shape that reproduces the observations reasonably well.

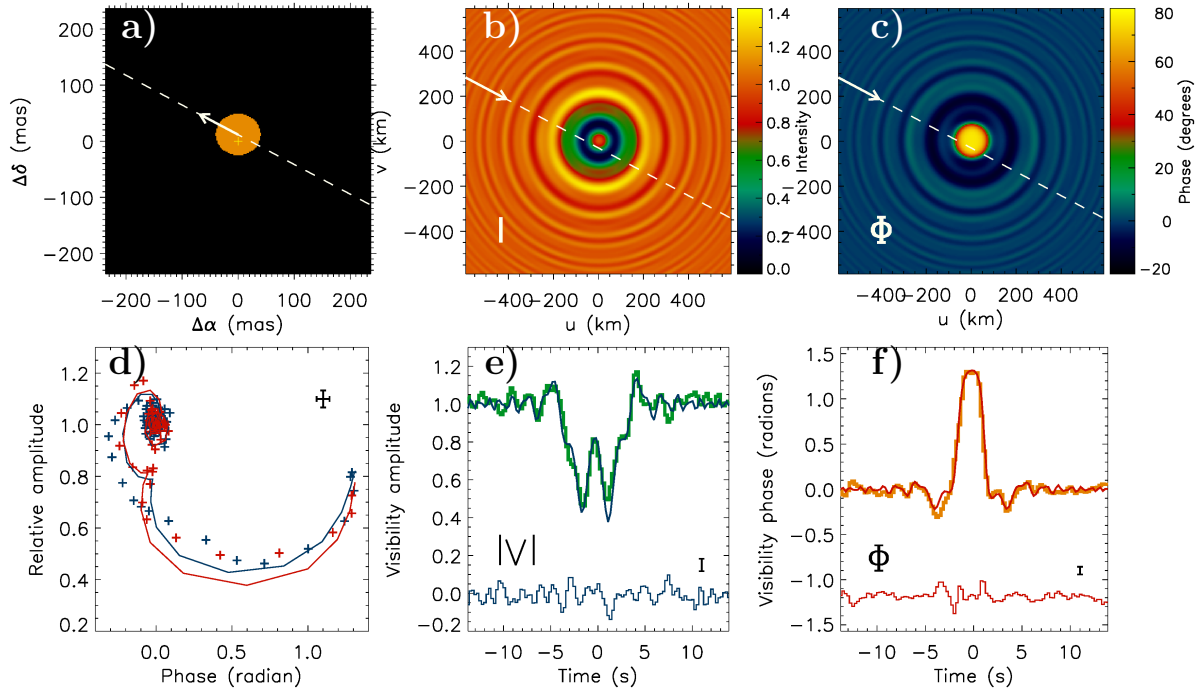


**Figure 9.** Best-fit ellipse-shaped model for Palma. The panels are same as in Fig. 4.

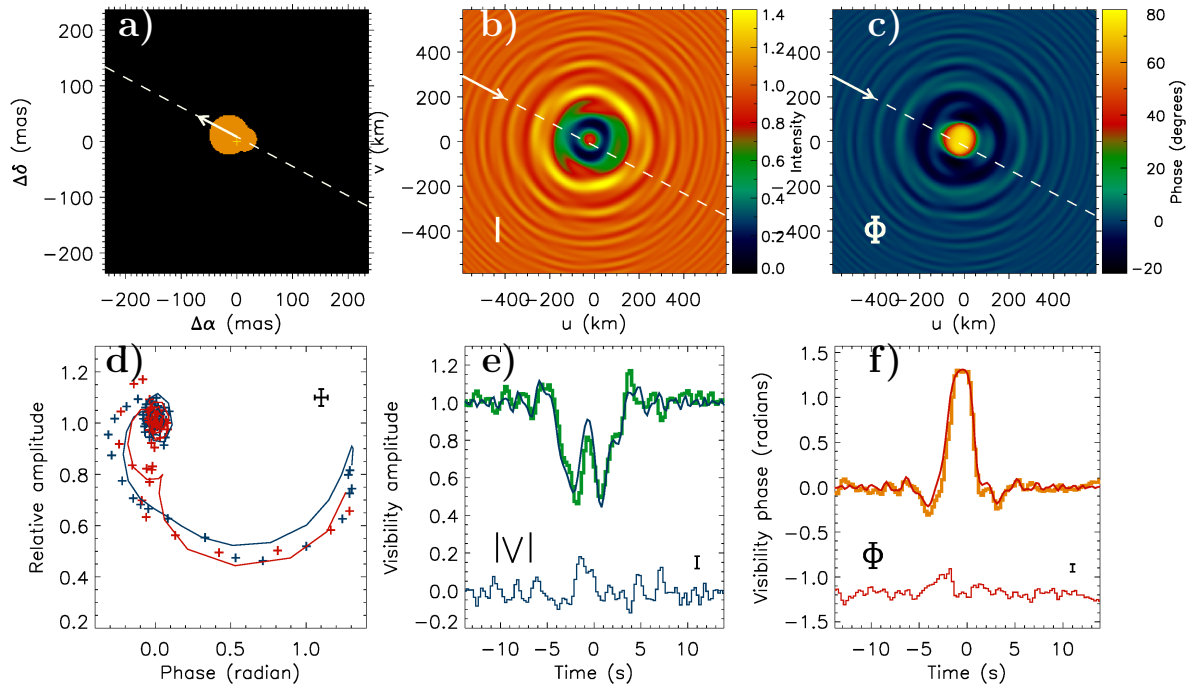


**Figure 10.** Best-fit potato-shaped binary model for Palma. The panels are same as in Fig. 4.

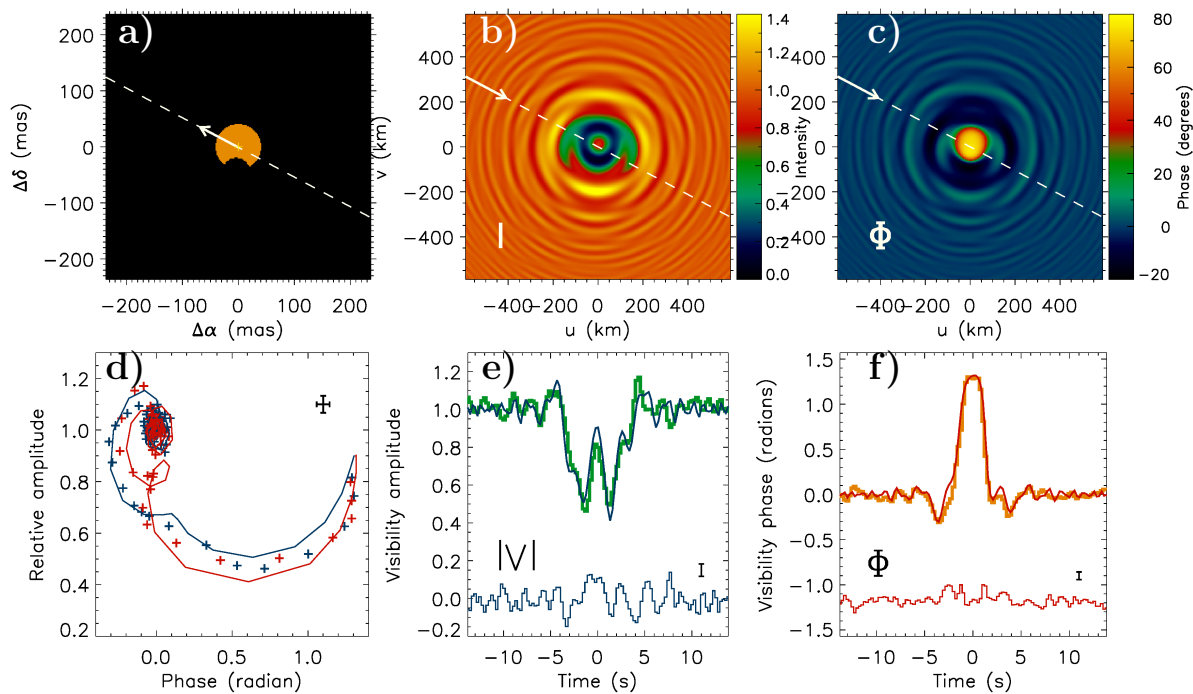


**Figure 11.** Best-fit curved model for Palma. The panels are same as in Fig. 4.

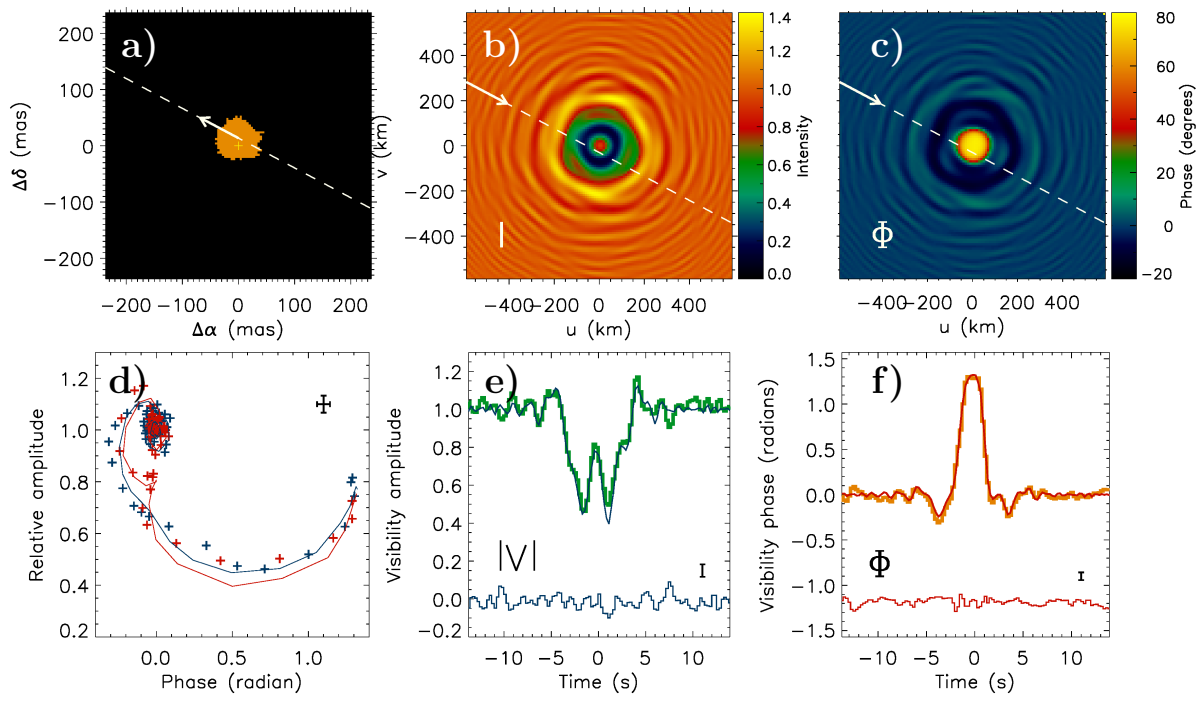


**Figure 12.** Random shape producing small residuals with  $\chi^2_{\nu} = 2.17$ . The ratio of the inscribed and circumscribed radii for this model is  $r = 0.75$ . The panels are same as in Fig. 4.